

Minimally Invasive Flexible Needle Manipulation Based on Finite Element Simulation and Cross Entropy Method

Yanzhou Wang¹, Chang Chang¹, Junling Mei², Simon Leonard³, and Iulian Iordachita¹

Abstract—We present a novel approach for minimally invasive flexible needle manipulations by pairing a real-time finite element simulator with the cross-entropy method. Additionally, we demonstrate how a kinematic-driven bang-bang controller can complement the control framework for better tracking performance. We show how electromagnetic (EM) tracking can be readily incorporated into the framework to provide controller feedback. Tissue phantom experiment with EM tracking shows the average targeting error is $0.16 \pm 0.29\text{mm}$.

I. INTRODUCTION

Percutaneous needle interventions capture a broad class of minimally invasive diagnosis and treatment procedures, such as biopsy [1]–[3], brachytherapy [4], [5], and spinal injection [6]–[8]. Depending on the clinical procedure, a range of needles with different gauges, stiffness levels, and tip geometries is available. These inherent needle characteristics play a crucial role in determining how the needle moves through soft biological tissues; additionally, surgeons also employ various techniques, such as rotating or bending the needle, to adjust the position of the needle tip *in situ* during insertion.

Knowledge of intricate needle-tissue interactions, as well as reliable trajectory planning and tracking algorithms are crucial to ensuring a minimally invasive insertion with high placement accuracy. A large amount of research conducted on needle insertion falls under *steering* of bevel-tip needles, where it is assumed that the needle follows its tip exactly and steering is achieved only via axial rotation [9]. Such assumption implies a low relative bending stiffness of the needle compared to its surrounding soft tissues, and inputs that actively change the shape of the needle cannot be taken into account. Needle *manipulation* solves another class of problem where the needle is modeled as a continuum, and inputs that actively changes the shape of the needle are also considered, such as base manipulation and lateral displacement using robotic devices [10]–[16]. Stemming from the field of solid mechanics and finite element methods, these models can capture a wide variety of input types and can

benefit particularly to sensory feedback along the needle, such as medical imaging [11], optical tracking [13], and fiber Bragg grating (FBG) optical sensors [15].

This paper demonstrates a flexible needle planning and control strategy for continuum needle models where the insertion dynamics is not readily captured by a kinematic model. More specifically, a finite element (FE) simulation is needed to capture complex nonlinear tissue behaviors and generic control actions along the length of the needle. Since the needle will be discretized into discrete elements, the complete state of the needle, and the simulation environment in general, could involve hundreds of variables, and planning for a minimally invasive insertion and closed-loop control of the flexible needle becomes a challenging problem.

Previous works in this domain focus primarily on resolved-rate control, which relies on inverting a numerical input-output Jacobian matrix obtained either via Broyden’s update law or simulating small input disturbances [10], [13], [15]–[18]. Yet obtaining such invertible mapping can be challenging, since it requires the system to have equal number of input and output variables, and can generate potentially dangerous needle manipulations that will cause tissue tearing [16]. Others investigate in the case of bevel-tip needles how to combine lateral actuation with axial rotation for the sole purpose of keeping the needle on a straight line [12], and they identified the phenomenon that lateral actuation has diminishing effect as the needle is embedded deeper into soft tissues, yet it remains to be seen how the two actions can be combined to reach arbitrary targets.

In this paper, we show how the cross entropy (CE) method can be readily coupled with a FE simulation of needle insertion for both path planning and closed-loop control for percutaneous interventions. In particular, we demonstrate in the case of a bevel-tip needle, how needle *manipulation* can be used together with *steering* to achieve a minimally invasive insertion, and how positional feedback can be seamlessly integrated with the current framework.

The rest of the paper is as follows. Section II introduces our realtime FE simulator. Section III explains how the CE method can be used effectively to design both a trajectory planner and a model predictive controller, and how kinematic needle models can be incorporated to improve controller performance. Section IV explains our choice of positional feedback to the controller framework and method of sensor characterization. Sections V and VI describe our experiments and summarize our findings.

This work is supported by NIH R01EB020667, R01EB036015, R01CA235134, and in part by a collaborative research agreement with the Multi-Scale Medical Robotics Center in Hong Kong.

¹Yanzhou Wang, Chang Chang, and Iulian Iordachita are with the Department of Mechanical Engineering and the Laboratory of Computational Sensing and Robotics, Johns Hopkins University, Baltimore, MD, USA. ywang521@jh.edu

²Junling Mei is with the Laboratory of Computational Sensing and Robotics, Johns Hopkins University, Baltimore, MD, USA.

³Simon Leonard is with the Department of Computer Science and the Laboratory of Computational Sensing and Robotics, Johns Hopkins University, Baltimore, MD, USA.

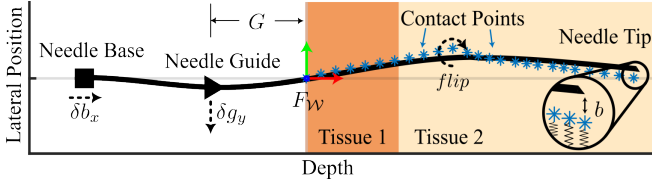


Fig. 1: Model schematic generated by the simulator. Three actions, δb_x , δg_y , and $flip$ correspond to needle insertion, needle guide translation, and bevel direction change, respectively. Needle guide is separated from skin entry point by distance G .

II. FINITE ELEMENT SIMULATOR

Bevel needle manipulation in multi-layered soft tissue environment is simulated in a mechanics-based FE simulator [19]. The simulator assumes a one-term Ogden hyper-elastic model for soft tissue layers. Needle tip geometry is controlled by placing a “pre-compressed spring” at the needle tip with a constant offset b (i.e. setting $b = 0$ simulates a symmetric-tip needle, see Fig. 1). This design choice couples needle bevel effect with tissue properties, and allows continuous simulation across different media, for example, from air into skin and muscle.

The state of the simulation is maintained by a tuple of needle state X and a list of contact points C . Evolution of the nonlinear system is represented by a difference equation

$$(X_{k+1}, C_{k+1}) = f(X_k, C_k, U_k), \quad (1)$$

where k represents the simulation step.

For an n -node discretization of the needle, needle state $X = [x_1, y_1, \theta_1, \dots, x_n, y_n, \theta_n, bvl]^\top \in \mathbb{R}^{3n} \times \mathbb{Z}_2$ consists of n needle nodal positions and orientations, with a binary variable $bvl = \{-1, 1\}$ indicating bevel direction. The list of contact points, C , is dynamically updated at every simulation step based on needle configuration.

Control inputs currently supported by the simulator are $U = [\delta b_x, \delta b_y, \delta b_\theta, \delta g_y, flip]^\top \in \mathbb{R}^4 \times \mathbb{Z}_2$, which denote needle (b)ase translations in the x and y directions and rotation θ , needle (g)uide translation in the y direction, as well as a binary signal $flip$ to change bevel direction.

The complete set of inputs generates redundancy in terms of needle configuration, and can trivialize planning problems. For example, a rigid transformation of the needle can be achieved by moving δb_y and δg_y in the same direction and by the same amount. Here, we choose a subset of three distinct and representative control inputs that affect needle trajectory in unique ways: $U = [\delta b_x, \delta g_y, flip]^\top \in \mathbb{R}^2 \times \mathbb{Z}_2$. Signal δb_x moves the entire needle in the direction of insertion, and the action follows the needle base during insertion; δg_y introduces needle bending by displacing part of the needle that is in contact with the movable guide, but the point of action is fixed relative to the insertion direction; finally, $flip$ is a binary signal and affects the needle shape only when the needle is in contact with soft tissue and $\delta b_x > 0$. Together, these three control inputs need to act simultaneously to achieve a minimally invasive insertion.

III. CROSS-ENTROPY METHOD

The number of states of the simulator in equation (1) changes dynamically depending on the insertion history, and can involve hundreds of state variables depending on mesh resolution and fineness of contact point formation. We show how the cross-entropy (CE) method is well-suited for working with the above system for both trajectory planning and tracking tasks.

Following the development of [20], we consider a needle insertion trajectory as a discretized sequence of $(m+1)$ states and controls over a fixed time interval $\tau = [0, T]$. From a given initial needle state X_0 , a control sequence $U : \tau \rightarrow \mathcal{U}$ forms a sequence of system states $X : \tau \rightarrow \mathcal{X}$ based on the system difference equation 1. The trajectory is denoted as $\pi : \tau \rightarrow \mathcal{U} \times \mathcal{X}$, with associated cost $J(\pi)$ defined in general as

$$J(\pi) = \sum_{s=0}^m \phi(\pi(s)) dt, \quad (2)$$

where $\pi(s) = (U(s), X(s))$ denotes a tuple of control-state pair at step s , $\phi(\cdot)$ a non-negative cost function, and dt a fixed time interval such that $s \cdot dt \in \tau$. In this work, we consider control “primitives” $z = \{U_s\}$ over dt , where each U_s , $0 \leq s \leq m$, is constant. We parameterize the importance density of z with a Gaussian distribution $p(z, v)$ from the parametric space $\mathcal{V} = \mathbb{R}^{n_z} \times \mathbb{R}^{(n_z^2 + n_z)/2}$ and with element $v = (\mu, \Sigma) \in \mathcal{V}$. In other words, independent and identically distributed (i.i.d.) random samples of control primitives Z_1, \dots, Z_N are drawn from the distribution $p(z, v)$, with mean μ and covariance Σ .

The CE approach executes a multi-level search based on the following: First, initialize counter $j = 1$, parameter $v_0 = (\mu_0, \Sigma_0)$ and cost threshold $\gamma_0 = \infty$, then

- 1) Sample Z_1, \dots, Z_N from $p(z, v_{j-1})$ and form a set of “elite” samples $\mathcal{E}_j = \{Z_i | J(Z_i) \leq \gamma_{j-1}\}$.
- 2) Calculate the ρ th quantile $\gamma_j = J_{[\rho N]}$ for a user-defined parameter ρ .
- 3) Update components of v_{j+1} based on equation (3).

$$v_j = \arg \max_v \frac{1}{N} \sum_{i=1}^N \mathbb{I}_{J(Z_i) \leq \gamma_j} \log p(Z_i, v_{j-1}), \quad (3)$$

where $\mathbb{I}(\cdot)$ is the indicator function. This process is repeated until convergence or when the algorithm reaches the maximum number of execution.

We consider a Gaussian distribution, therefore equation (3) becomes equations (4) and (5).

$$\mu_j = \frac{1}{|\mathcal{E}_j|} \sum_{Z_k \in \mathcal{E}_j} Z_k, \quad (4)$$

$$\Sigma_j = \frac{1}{|\mathcal{E}_j|} \sum_{Z_k \in \mathcal{E}_j} (Z_k - \mu_j)(Z_k - \mu_j)^\top. \quad (5)$$

A. Offline Surgical Planning

For a minimally invasive needle insertion, we desire high targeting accuracy with small tissue compression and few bevel rotations to prevent unnecessary tissue tearing and

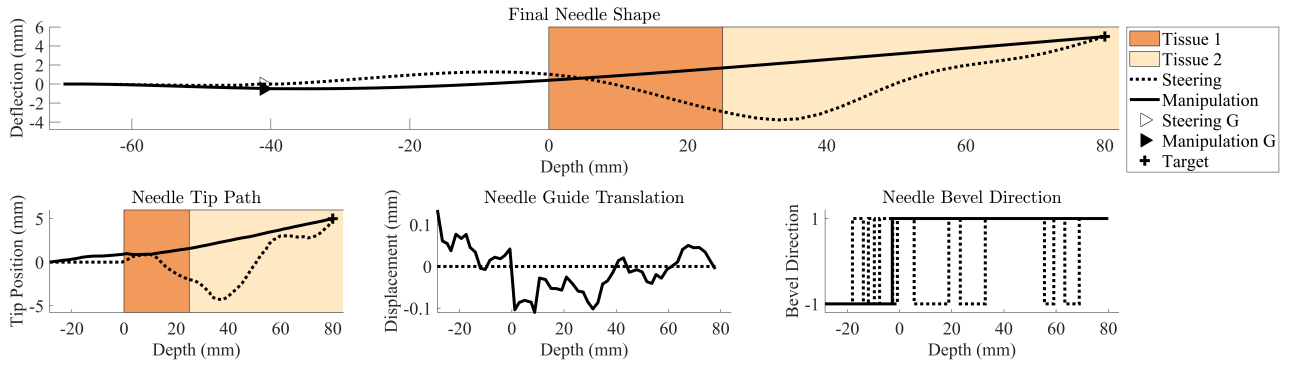


Fig. 2: Insertion plans returned by CE using *manipulation* and *steering* strategies. The *manipulation* strategy attempts to find a non-zero insertion angle such that needle bevel can be effectively used to steer towards target, while a pure *steering* strategy relies only on changing of bevel direction to achieve steering.

removal. For a single insertion, the planning cost J^P is the summation of individual step costs J_s and the final cost J_f , and equation (2) takes the form

$$J^P(\pi) = J_f(\pi_f) + \sum_{s=0}^m J_s(\pi_s). \quad (6)$$

The step cost is defined in quadratic form

$$J_s(\pi_s) = (X_s^\top Q X_s + U_s^\top R U_s) \mathcal{H}(X_s) dt, \quad (7)$$

where Q penalizes large needle deflections from an initially straight profile, R penalizes needle manipulations that can potentially be harmful to soft tissues, particularly needle guide translation and bevel direction change. Binary action *flip* can be optimized by taking the sign of a nonzero numerical value, ϵ , and $flip = \text{sign}(\epsilon)$.

The step cost is activated by a Heaviside function $\mathcal{H}(X)$ when the needle comes into contact with soft tissue. Final cost is defined at the end of the trajectory, and weighted by constants γ_1, γ_2 between targeting accuracy $\|P_{tip} - P_{target}\|_2$ and tissue strain energy \mathcal{W} :

$$J_f(\pi_f) = \gamma_1 \|P_{tip}(X) - P_{target}\|_2 + \gamma_2 \mathcal{W}, \quad (8)$$

where P_{tip} and P_{target} denote needle tip position and target position, respectively. Tissue strain energy \mathcal{W} can be calculated using the one-term Ogden hyperelastic model and tissue properties described in [18]. In short, since the simulator keeps track of a list of active contact points C ,

$$\mathcal{W} = \sum_{c \in C} w_c \frac{2\mu_c}{\alpha_c^2} (2\lambda_{1,3}^{\alpha_c} + \lambda_2^{\alpha_c} - 3), \quad (9)$$

for each contact point c . Tissue model parameters μ, α are defined on a per-layer basis based on the location of contact points. Stretch ratios λ_i are calculated at each contact point with respect to the corresponding needle deflection. Unconfined uniaxial compression is assumed and λ_2 is assigned as the principal stretch ratio. Constants w_c are optional weighting factors for different tissue layers.

Planning phase returns a minimally invasive trajectory $\bar{\pi}$, that consists of an optimal control sequence \bar{U} and associated

needle states \bar{X} . These nominal values are used to warm start the online trajectory tracking algorithm derived from the same CE framework.

A kinematic-like *steering* plan can be trivially obtained by lowering the needle bending stiffness in the simulator and zeroing the covariance entries that correspond to inputs that actively change the needle shape. A comparison of optimal plans of the two strategies is shown in Fig. 2. Note that since bevel effect is coupled with tissue stiffness, needle *manipulation* can affect needle shape and trajectory before the needle touches soft tissue. In this work, we focus on needle *manipulation*, but we show in Sec. III-B.2 how to bridge kinematic models for trajectory tracking.

B. Online Trajectory Tracking

To track the nominal trajectory subject to uncertainties in initial conditions and model parameters, we extend the CE optimization framework to make a model predictive controller (MPC) for continuous input signal generation. We further couple it with an “ad hoc” bang-bang controller to switch bevel tip directions.

1) *Model Predictive Controller*: The CE optimization framework can be extended to build an MPC for online trajectory tracking. The underlying idea is to execute a single control input U sampled from \bar{U} that minimizes tracking error within a short window in a receding-horizon fashion.

We consider a moving window $\tau' \subset \tau$ with the same discrete time step dt . To warm start the algorithm, we set the new sample mean $\mu' = \bar{U}' \subset \bar{U}$ within the time window. The covariance matrix Σ' is re-initiated depending on the noise of the environment and discrepancy of the needle initial conditions, and the algorithm introduced in Sec. III is applied to get the next control input.

The nominal trajectory \bar{X} contains not only the needle tip position P_{path} , but also the tip orientation θ_{path} returned by the simulator. For off-the-shelf needles, tip orientation plays an active role in terms of long-term needle trajectory, and is important to track if possible [16]. Therefore, considering the needle tip state $g(X) = (x_n, y_n, \theta_n) \in SE(2)$, trajectory tracking cost J^t is the cumulative deviation from the nominal

path $\bar{g}(\bar{X})$ over the short horizon τ' according to

$$J^t(\pi, \bar{\pi}) = \sum_{s'=0}^{m'} d_{s'}(g, \bar{g})_W dt, \quad (10)$$

where $s'dt \in \tau'$, and $d(\cdot, \cdot)_W : SE(2) \times SE(2) \rightarrow \mathbb{R}$ assigns a cost to the deviation based on weight W .

Contrary to planning, the MPC is only in charge of continuous input signals. Binary input signal, $flip$, is generated by a bang-bang controller derived from a kinematic model.

2) *Kinematic-based Bang-Bang Controller*: The necessity of the bang-bang controller is as follows. First, given the current set of U , needle tip position and orientation cannot be independently controlled, therefore even if the MPC can correct the initial tip position deviation while the needle is in air, the needle will enter soft tissue at a different angle from the plan, and vice versa. Second, in an environment where the relative stiffness between needle and tissue is high, bevel effect is diminished until the inserted depth becomes large and needle motion appears nonholonomic. These two issues present a major challenge to the MPC since inherently a short trajectory window is considered, which can put the needle in an irrecoverable state.

The bang-bang controller assumes a kinematic model using the current needle tip configuration $g(X)$ based on the following discrete kinematic equation

$$\begin{bmatrix} x_{n,k+1} \\ y_{n,k+1} \\ \theta_{n,k+1} \end{bmatrix} = \begin{bmatrix} x_{n,k} \\ y_{n,k} \\ \theta_{n,k} \end{bmatrix} + \begin{bmatrix} \cos(\theta_{n,k}) \\ \sin(\theta_{n,k}) \\ sgn \cdot \kappa \end{bmatrix} u, \quad (11)$$

where $sgn \in [bvl, -bvl]$ takes either the current bevel direction or its opposite, κ is a small positive value that will generate a curved path with direction determined by sgn . The continuous insertion signal δb_x obtained by the MPC is divided into smaller steps, which are u in the above equation.

Since sgn can only take two values, two needle tip trajectories will be generated. Decision $flip$ is then based on the trajectory that brings the needle tip closer to the final target position. In other words, if we define the tip position at the end of kinematic trajectory generated by choosing bevel direction sgn as P_{tip}^{sgn} , then

$$bvl^* = \arg \min_{sgn} \|P_{tip}^{sgn}(X) - P_{target}\|_2, \quad (12)$$

$$flip = \begin{cases} -1, & \text{if } bvl^* = bvl \\ 1, & \text{otherwise.} \end{cases} \quad (13)$$

The reason for using P_{target} instead of P_{path} in equation (12) is to introduce long-horizon prediction so that the bevel tip always points in the direction of target, instead of chasing the nominal path by introducing frequent bevel direction changes.

IV. CONTROLLER FEEDBACK

Common feedback modalities that fit within the proposed control framework include electromagnetic (EM) tracking, medical imaging, as well as FBG. An EM sensor can be

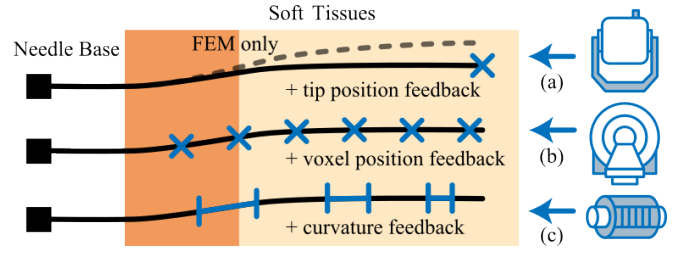


Fig. 3: Comparison between different feedback modalities: (a) EM tracking, (b) medical imaging, and (c) fiber Bragg grating with the proposed FE-based framework.

attached to the needle to provide a single position and orientation feedback in high frequency, while medical imaging can provide approximate positional information along the length of the needle, subject to image resolution, speed of acquisition, and accuracy of image segmentation. FBG sensors can be embedded in the needle to provide partial shape information in real time [15]. A pictorial comparison between different feedback modalities compatible with the presented framework is shown in Fig. 3.

A. Position Feedback with EM Tracking

In this work, we use an EM sensor coil embedded at the tip of an 21 gauge needle with 0.819mm outer diameter (Aurora, NDI Digital, Canada) to provide position feedback, which is treated as an essential boundary condition in the FE solver. Although it is possible to incorporate sensor orientation information, considering the generalizability of proposed approach to medical imaging, orientation would be challenging to extract precisely. Therefore, only tip position is used as feedback.

B. EM Noise and Accuracy Evaluation

The choice of using EM tracking is motivated by its speed and accuracy within a “good” measurement window; however, EM sensors are vulnerable to field distortions introduced by components of the needle driver and devices commonly found in the operating room (OR). While the operating environment recommended by the manufacturer should be clear of any ferromagnetic object within 1m of the EM field generator [21], such requirement is unrealistic in any OR.

In order to define an operating window for position tracking and to incorporate the tracking device into our setup, an evaluation of the accuracy of the 5-degree-of-freedom (DOF) needle tip tracker and 6DOF reference trackers (Aurora, NDI Digital, Canada) is performed.

We attach both the 5DOF tip tracker and a 6DOF reference tracker onto a motorized XYZ linear stage assembly. By repeatedly adjusting the positions of the two sensors with the linear stage and calculating the measurement error, we find that a minimum distance of 70cm between the field generator and the linear stage is required to achieve an overall root mean square error (RMSE) of 0.17mm and 0.25mm for the two sensors, respectively, which are lower than the

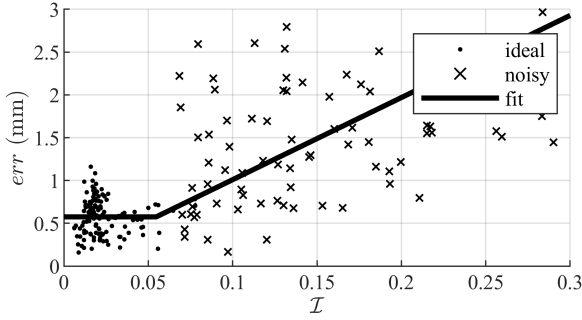


Fig. 4: Indicator value correlates measurement error in a piecewise linear fashion. Indicator values beyond 0.3 are not shown to better visualize data in the *ideal* environment.

manufacturer-reported RMSE of 0.70mm and 0.48mm [21]. Since no other metallic and power sources are present in the setup, we call this the *ideal* environment.

Each 6DOF reference tracker consists of two 5DOF sensors and returns an indicator \mathcal{I} from 0 to 9.9 to indicate field distortion. To find the correlation between measurement error and \mathcal{I} , we use the linear stages to move the sensors on an $5 \times 5 \times 5$ square grid within a 1000cm^3 volume, with 100 position measurements collected at each grid point. The data collection process is repeated for 5 times, therefore a total of $M = 500$ measurements are collected at each of $N = 125$ grid points. Furthermore, we deliberately introduce additional field distortion by placing a metal plate underneath the setup. We call this the *noisy* environment.

For each EM measurement, $\tilde{P}_{i,j}$ represents position at the i th grid point out of N grid points, and the j th measurement out of M total samples. The mean position of the M samples at the i th grid point can be calculated as

$$\bar{P}_i = \frac{1}{M} \sum_{j=1}^M \tilde{P}_{i,j}. \quad (14)$$

Since we treat the grid points formed by the linear stage as true positions P_i , measurement error is defined as the Euclidean distance between the measured mean position and the ground truth position

$$err_i = \|\bar{P}_i - P_i\|_2, \quad (15)$$

and the RMSE of all N grid points in a given environment can be obtained by

$$rmse = \sqrt{\frac{\sum_{i=1}^N err_i^2}{N}}. \quad (16)$$

TABLE I: Sensor Measurement Errors

Error (mm)	5DOF Tip				6DOF Ref.			
	<i>rmse</i>	95% ^{a)}	max	<i>jitter</i>	<i>rmse</i>	95% ^{a)}	max	<i>jitter</i>
Official	0.70	1.40	-	-	0.48	0.88	-	-
ideal	0.65	1.10	1.40	0.07	0.61	0.91	1.16	0.08
noisy	1.53	3.20	4.36	0.04	2.70	5.27	8.16	0.07

a) 95% confidence interval

TABLE II: Indicator Value, \mathcal{I}

\mathcal{I}	mean	sd	max	min
ideal	0.0239	0.0138	0.0779	0.0061
noisy	0.1944	0.1049	0.4784	0.0684

Similarly, since multiple samples are taken at each grid point, sensor jitter in a given environment can be evaluated with

$$jitter = \sqrt{\frac{\sum_{i=1}^N \sum_{j=1}^M \|\bar{P}_i - \tilde{P}_{i,j}\|_2^2}{NM}}. \quad (17)$$

As shown in Table I, in the ideal environment, the RMSE is consistent with the official product specifications [21]. When the metal plate is introduced and environment becomes noisy, the respective maximum errors of the two sensors rise to 4.36mm and 8.16mm, but jitter does not have a significant difference in the noisy environment. The reason for the accuracy of the tip being higher than that of the reference can be attributed to the needle tip being closer to the field generator in our setup [22].

As shown in Fig. 4, a piecewise linear fit suggests that in the ideal environment, $err = 0.575 \pm 0.211\text{mm}$; in the noisy environment, $err = 9.591\mathcal{I} + 0.051\text{mm}$. We take the indicator value $\mathcal{I} = 0.0547$, which is the 95 percentile of \mathcal{I} measured in the ideal environment, as a good representation of a rather noise-less environment. This choice is further corroborated by Table II, which shows that in the noisy environment, $\min \mathcal{I} > 0.0547$. This threshold value is used in our setup, where three reference markers are placed around the tissue phantom in order to estimate noise magnitude around the needle workspace, and keep all three indicator values below the threshold.

V. PHANTOM EXPERIMENT WITH EM FEEDBACK

Phantom experiments are performed with hardware setup shown in Fig. 5. The 2DOF needle driver provides translation

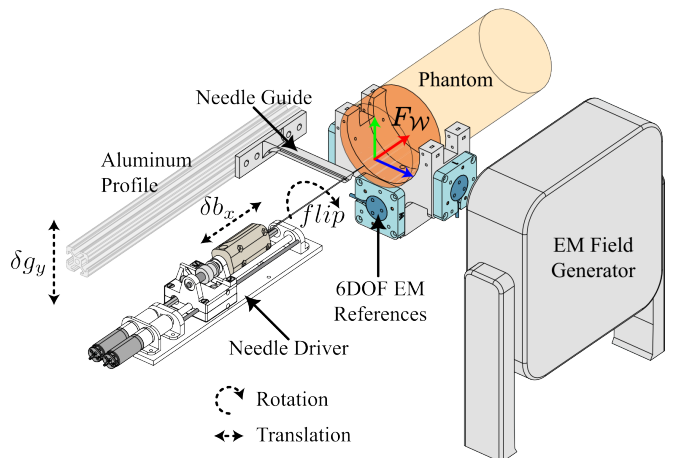


Fig. 5: Tissue phantom experiment setup. Needle driver generates δb_x and *flip*, and linear stage (not shown) generates needle guide δg_y attached to the aluminum profile. Three EM reference markers are used to monitor field distortion.

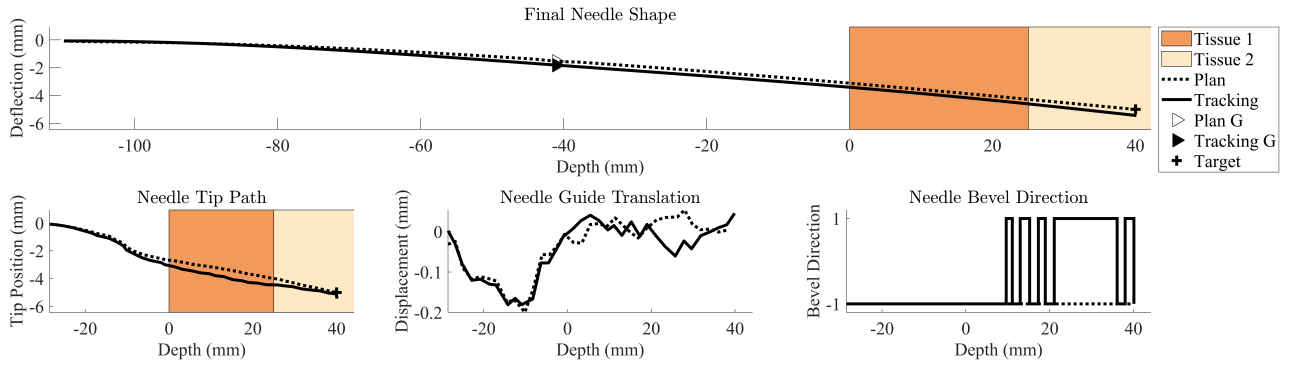


Fig. 6: Needle insertion planning and tracking for target located 40mm deep with 5mm offset from needle initial configuration.

distance up to 110mm, with rotation limited to 0° and 180° to replicate the simulator setup. The movable needle guide is actuated by the same linear stage used in Sec. IV-B, and is attached to an aluminum profile in order to reduce electromagnetic interference. All motors are controlled independently by a motion controller (DMC-4143, Galil Motion Control, USA), and cross-platform communication is established using ROS2 [23]. When the hardware system is powered on and placed in an ideal environment, $\mathcal{I} = 0.04$, proving EM compatibility of our system.

Tissue phantom used in the experiment has two layers of different stiffness values. The superficial and deep layers are assigned Ogden model parameter $\mu_1 = 1.82\text{kPa}$ and $\mu_2 = 3.63\text{kPa}$, respectively, with $\alpha = 8.74$ for both layers [15]. Needle Young's modulus is set to 200GPa for stainless steel. The needle guide is positioned at $G = 41\text{mm}$ with initial tip-to-skin distance of 28.5mm. Target depths are chosen to be from 25mm to 45mm in 5mm increments to simulate a lumbar injection scenario, where the average insertion depths is $36.7 \pm 9.9\text{mm}$ [24]. With the 21 gauge bevel tip needle initially aligned with 0mm lateral axis, we also target positions with $\pm 5\text{mm}$ lateral variations to simulate initial registration errors and misalignment. Fifteen targets in total are selected and ten insertions are performed on each target.

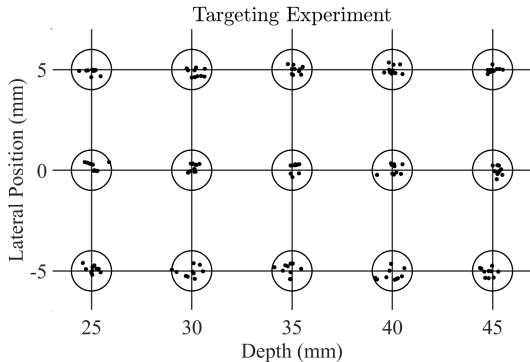


Fig. 7: Targeting experiment with guide-to-skin distance $G = 41\text{mm}$. Targets are shown as the center of circles, which have radius of 1mm. Black dots show the needle tip position reported by EM tracker.

VI. RESULTS AND DISCUSSION

An example insertion for the proposed planning and control framework is shown in Fig. 6. Notably, for targets with large offset from the needle initial configuration, the proposed framework is able to take advantage of the gap between needle tip and entry point to perform the most correction in air, and the controller is able to generate needle guide motions that closely resembles the plan.

Once the needle touches the tissue, the CE-driven MPC and kinematic-driven bang-bang controller is able to work together, adjusting the guide position and bevel direction as needed. There are, however, more bevel direction changes in close proximity with each other, which can be undesirable depending on the specific clinical scenario. This is in part due to the needle not rotating axially in place such that changing the bevel direction also changes the tip position. Reducing the curvature value κ or implementing an error threshold in equation (12) can mitigate this issue.

Through experimentation, we decide that needle orientation upon entering the tissue is more important than position, particularly in determining long-term tracking performance. Since the set of control inputs considered in the present case (see Fig. 1) cannot independently control tip position and orientation, higher weight is given to needle tip orientation, which explains the non-zero tracking error at the tip near the needle entry point. The overall performance is shown in in Fig. 7. Target positions are centers of the circles, which have radius of 1mm. Final needle tip positions are represented as dots. The average targeting error is $0.16 \pm 0.29\text{mm}$ based on the final position returned by the tip tracker.

VII. CONCLUSION AND FUTURE WORK

We demonstrate an effective integration of the CE method with a real-time FE simulator for minimally invasive needle manipulation planning and tracking. Our approach leverages a CE-driven MPC in conjunction with a kinematic-driven bang-bang controller to achieve precise needle insertions. Tissue phantom experiment reveals targeting accuracy is within 1mm of various targets. Future research will focus on extensive experiments with real soft tissues and needles of different gauges, as well as impacts of variations in guide-to-skin distance and fusion with medical images.

REFERENCES

- [1] P. P. Bourgouin, K. J. Rodriguez, and F. J. Fintelmann, "Image-guided percutaneous lung needle biopsy: how we do it," *Techniques in Vascular and Interventional Radiology*, vol. 24, no. 3, p. 100770, 2021.
- [2] E. Birgin, C. Yang, S. Hetjens, C. Reissfelder, P. Hohenberger, and N. N. Rahbari, "Core needle biopsy versus incisional biopsy for differentiation of soft-tissue sarcomas: a systematic review and meta-analysis," *Cancer*, vol. 126, no. 9, pp. 1917–1928, 2020.
- [3] R. A. Sheth, M. O. Baerlocher, B. L. Connolly, S. R. Dariushnia, P. B. Shyn, S. Vatsky, A. L. Tam, and S. Gupta, "Society of interventional radiology quality improvement standards on percutaneous needle biopsy in adult and pediatric patients," *Journal of Vascular and Interventional Radiology*, vol. 31, no. 11, pp. 1840–1848, 2020.
- [4] C. Chargari, E. Deutsch, P. Blanchard, S. Gouy, H. Martelli, F. Guérin, I. Dumas, A. Bossi, P. Morice, A. N. Viswanathan, *et al.*, "Brachytherapy: An overview for clinicians," *CA: a cancer journal for clinicians*, vol. 69, no. 5, pp. 386–401, 2019.
- [5] H. Ragde, G. L. Grado, B. Nadir, and A.-A. Elgamal, "Modern prostate brachytherapy," *CA: A Cancer Journal for Clinicians*, vol. 50, no. 6, pp. 380–393, 2000.
- [6] H.-S. Won, M. Yang, and Y.-D. Kim, "Facet joint injections for management of low back pain: a clinically focused review," *Anesthesia & Pain Medicine*, vol. 15, no. 1, pp. 8–18, 2020.
- [7] L. Manchikanti, N. N. Knezevic, A. Navani, P. J. Christo, G. Limerick, A. K. Calodney, J. Grider, M. E. Harned, L. Cintron, C. G. Gharibo, *et al.*, "Epidural interventions in the management of chronic spinal pain: American society of interventional pain physicians (asipp) comprehensive evidence-based guidelines," *Pain physician*, vol. 24, no. S1, p. 27, 2021.
- [8] M. Carassiti, G. Pascarella, A. Strumia, F. Russo, G. F. Papalia, R. Cataldo, F. Gargano, F. Costa, M. Pierri, F. De Tommasi, *et al.*, "Epidural steroid injections for low back pain: A narrative review," *International Journal of Environmental Research and Public Health*, vol. 19, no. 1, p. 231, 2021.
- [9] Y. Li, C. Yang, A. Bahl, R. Persad, and C. Melhuish, "A review on the techniques used in prostate brachytherapy," *Cognitive Computation and Systems*, vol. 4, no. 4, pp. 317–328, 2022.
- [10] S. DiMaio and S. Salcudean, "Needle steering and motion planning in soft tissues," *IEEE Transactions on Biomedical Engineering*, vol. 52, no. 6, pp. 965–974, 2005.
- [11] D. Glozman and M. Shoham, "Image-guided robotic flexible needle steering," *IEEE Transactions on Robotics*, vol. 23, no. 3, pp. 459–467, 2007.
- [12] T. Lehmann, C. Rossa, N. Usmani, R. Sloboda, and M. Tavakoli, "Deflection modeling for a needle actuated by lateral force and axial rotation during insertion in soft phantom tissue," *Mechatronics*, vol. 48, pp. 42–53, 2017.
- [13] Y. Adagolodjo, L. Goffin, M. De Mathelin, and H. Courtecuisse, "Robotic insertion of flexible needle in deformable structures using inverse finite-element simulation," *IEEE Transactions on Robotics*, vol. 35, no. 3, pp. 697–708, 2019.
- [14] Y. Wang, Y. Xu, K.-W. Kwok, and I. Iordachita, "In situ flexible needle adjustment towards mri-guided spinal injections based on finite element simulation," in *2023 International Symposium on Medical Robotics (ISMR)*, pp. 1–7, 2023.
- [15] Y. Wang, Y. Xu, J. Kang, J. Fritz, and I. Iordachita, "Simulation-based flexible needle control with single-core fbg feedback for spinal injections," *IEEE Transactions on Medical Robotics and Bionics*, vol. 6, no. 3, pp. 1073–1083, 2024.
- [16] Y. Wang, L. Al-Zogbi, J. Liu, L. Shepard, A. Ghazi, J. Tokuda, S. Leonard, A. Krieger, and I. Iordachita, "Shape manipulation of bevel-tip needles for prostate biopsy procedures: A comparison of two resolved-rate controllers," *arXiv preprint arXiv:2402.03125*, 2024.
- [17] M. C. Bernardes, P. Moreira, L. Mareschal, C. Tempany, K. Tuncali, N. Hata, and J. Tokuda, "Data-driven adaptive needle insertion assist for transperineal prostate interventions," *Physics in Medicine & Biology*, vol. 68, no. 10, p. 105016, 2023.
- [18] Y. Wang, K.-W. Kwok, K. Cleary, R. H. Taylor, and I. Iordachita, "Flexible needle bending model for spinal injection procedures," *IEEE Robotics and Automation Letters*, vol. 8, no. 3, pp. 1343–1350, 2023.
- [19] Y. Wang, L. Al-Zogbi, G. Liu, J. Liu, J. Tokuda, A. Krieger, and I. Iordachita, "Bevel-tip needle deflection modeling, simulation, and validation in multi-layer tissues," in *2024 IEEE International Conference on Robotics and Automation (ICRA)*, pp. 11598–11604, 2024.
- [20] M. Kobilarov, "Cross-entropy motion planning," *The International Journal of Robotics Research*, vol. 31, no. 7, pp. 855–871, 2012.
- [21] NDI, "Aurora v2 user guide, rev. 5," *1*, pp. 17–19, 2013.
- [22] M. Nakamoto, Y. Sato, Y. Tamaki, H. Nagano, M. Miyamoto, T. Sasama, M. Monden, and S. Tamura, "Magneto-optic hybrid 3-d sensor for surgical navigation," in *Medical Image Computing and Computer-Assisted Intervention—MICCAI 2000: Third International Conference, Pittsburgh, PA, USA, October 11-14, 2000. Proceedings 3*, pp. 839–848, Springer, 2000.
- [23] S. Macenski, T. Foote, B. Gerkey, C. Lalancette, and W. Woodall, "Robot operating system 2: Design, architecture, and uses in the wild," *Science robotics*, vol. 7, no. 66, p. eabm6074, 2022.
- [24] J. Fritz, P. U-Thainual, T. Ungi, A. J. Flammang, N. B. Cho, G. Fichtinger, I. I. Iordachita, and J. A. Carrino, "Augmented reality visualization with image overlay for mri-guided intervention: accuracy for lumbar spinal procedures with a 1.5-t mri system," *American Journal of Roentgenology*, vol. 198, no. 3, pp. W266–W273, 2012.